Unraveling high-pressure gas storage mechanisms in shale nanopores through SANS

Rui Zhang[1], Shimin Liu[1,*], Long Fan[1], Tomasz P. Blach[2], and Guijie Sang[1,#]

[1]Department of Energy and Mineral Engineering, G[3] Center and Energy Institute, The Pennsylvania State University, University Park, PA 16802, USA
[2]School of Minerals and Energy Resources Engineering, University of New South Wales, Sydney, NSW 2052, Australia
[#]Present address: Department of Civil and Environmental Engineering, University of Strathclyde, Glasgow G1 1XQ, UK

Corresponding Author:
[*]Email: szl3@psu.edu (S.L.)

Abstract

As storage rocks rather than source rocks, shale reservoirs can become a target to store methane in terms of energy security and sequester CO_2 in the long-term to mitigate climate change. Despite extensive studies investigating geochemical and geophysical properties of shale and gas adsorption and transport in shale matrix, limited studies have been devoted to characterizing nanoscale gas storage mechanisms in shale at high pressure. In this study, contrast-matching small-angle neutron scattering (SANS) has been conducted to quantify the gas storage mechanisms and capacity in three shale samples up to elevated high pressure. The estimated average scattering length density (SLD) in pores is smaller than the SLD of bulk phase at the pressure between 100 bar and the contrast-matched point (~600-700 bar), indicating a lower average adsorbed phase density in the pressure range for the measured shale samples. Three essential factors, including the final injection pressure, total organic carbon (TOC), and the accessible porosity, have been determined to screen a potential targeted shale reservoir and maximize methane storage and long-term CO_2 sequestration.

Keywords: Shale; nanoscale; gas storage and sequestration; contrast-matching SANS; adsorption

1. Introduction

Among the energy sources, natural gas is considered an abundant, reliable, and clean energy [1]. Due to the technical maturity of horizontal well drilling and hydraulic fracturing [2], natural gas exploitation and development in the United States have been heavily focused on shale reservoirs in recent decades [3]. Although commercial development of shale gas reservoirs has been conducted in the last decades, fluid transport dynamics in shale remain poorly understood with many specificities left unexplained [4]. One of the critical challenges for long-term shale gas production optimization is lacking reliable multi-scale and multi-mechanics gas transport model [4]. Meanwhile, the increasing trend of anthropogenic greenhouse gas emissions, *e.g.*, methane and CO_2, is alarming for global warming and its associated climate change [5]. One reason for the increase of atmospheric CO_2 concentration is the power generation by burning fossil fuels, which has adverse effects on the earth's ecological environment due to the raises of the global average temperature [5]. Net emission of CO_2 must approach zero to meet the Paris Agreement's criteria of limiting the increase of global temperature within 2 °C or 1.5 °C above pre-industrial levels [6]. According to the Research Agenda for CO_2 removal and reliable sequestration [6], several feasible negative-emission technologies and research & development plans have been identified, including (1) biological CO_2 sequestration in soils, forests, and wetlands; (2) synchronized bioenergy production and CO_2 capture; (3) coupling direct-air-capture and geological sequestration; and (4) enhancing geologic carbon mineralization or "weathering". CO_2-enhanced shale gas recovery and CO_2 sequestration in depleted shale gas reservoirs could be the cost-effective strategy to permenently store densified CO_2 in subsurface shale formations. With various mineral and organic matters, shale rock has hierarchical pore structures, including micro-fractures and macro-/meso-/micro-pores [7-11]. Methane or CO_2 is primarily stored as a free phase through the gas compression

in fracture voids and macropores, and as both bulk and adsorbed phases in meso-/micropores in shales [12, 13]. In general, the gas sorption capacity in shale is low due to the low total organic carbon (TOC) content [12-15]. And the adsorbed phase density is usually obtained either by using an empirical value [13, 16] or curve-fitting [16, 17] or analytical/molecular simulation methods [18, 19], which could cause inaccuracy to determine the real sorption capacity for a given *in situ* pressure and temperature conditions. The total gas storage capacity in shale is the sum of bulk phase and adsorbed phase gases. Therefore, understanding the gas storage behaviors in shale nanopores has practical applications on gas transport modeling and the estimation of the potential of methane or carbon storage in shale reservoirs.[20] The understanding could determine the injection rate and the potential of CO_2 sequestration in shale reservoirs to meet the challenge of climate change mitigation [21].

Numerous techniques can be successfully used to characterize pore structure in shale [22, 23], specified as invasive and noninvasive methods. However, only a limited number of studies have been devoted to characterizing gas storage and condensation behaviors in shale nanopores under *in situ* pressure and temperature conditions. Fortunately, small-angle neutron scattering (SANS) can be used to noninvasively quantify the structures of total nanopores in shale [24-27]. Combining SANS with the contrast-matching method, or so-called contrast-matching SANS, pore accessibility [10, 28-30] and gas behaviors in pores [31, 32] can be invasively quantified. Therefore, contrast-matching SANS is an excellent choice to determine gas storage behaviors in shale confined nanopores under *in situ* gas injection [33]. This study focuses on the characterization of nanopore structures of three shale samples and gas storage behaviors in accessible nanopores through *in situ* contrast-matching SANS measurements. CD_4 injection was used in this study because high-pressure CD_4 can have a relatively high scattering length density (SLD) than CO_2

which can reach or approach the contrast-matched condition of the shale samples with relatively high SLDs. We found that the Illinois shale sample with the highest TOC has the lowest pore accessibility. As the increase of injection gas pressure, adsorbed methane density in shale nanopores is found to be higher than bulk phase at relatively low pressure, lower than bulk phase at relatively high pressure, and again higher than bulk phase at even higher pressure. TOC could be the determining factor of gas storage in micropores because of the high affinity of gas leading to high adsorption. For free compression gas storage, accessible porosity of macro-/mesopores is found to be the leading controlling factor of total gas storage capacity. Apparently, the total gas storage will depend on the final equilibrium pressure in shale reservoirs. We believe the current research will improve fundamental understandings on methane storage and long-term CO_2 sequestration in shale reservoirs.

2. Materials and methods

2.1 Sample preparation and characterization

Three shale powder samples, pulverized to 60-80 mesh sizes (0.177-0.25 mm), were prepared from fresh block samples collected from different shale formations, including Marcellus Formation in Pennsylvania, USA, Illinois Basin in Indiana, USA, and Longmaxi Formation in Sichuan, China. Marcellus Formation describes the upper Eifelian and lower Givetian stage mudrock-dominated strata lying in the Middle Devonian timescale.[34] The shale outcrop fresh blocks were obtained in Frankstown, Pennsylvania. The collected shale in Illinois Basin is a roof shale above the Coal V (Springfield Coal Member, Petersburg Formation, Pennsylvania System) or so-called Springfield coal and below the Alum Cave Limestone Member, Dugger Formation.[35, 36] The roof shale is a black fissile marine shale.[35, 36] The roof shale fresh blocks were obtained from Bear Run Surface Mine in Carlisle, Indiana. Longmaxi Formation located in the Yangtze

area is in the Lower Silurian timescale.[37] The shale outcrop fresh blocks were obtained in Yibin, Sichuan, China.

The pulverized samples were oven-dried for 24 hours at 80°C, and all the dried samples were sealed in the air-tight Ziploc bags before the contrast-matching SANS and the sorption/diffusion measurements. X-ray diffraction (XRD) and LECO CS230 carbon/sulfur determinator were conducted to obtain the mineralogical information and the TOC of the samples, respectively, as shown in Table S2 in the SI. We can find that the Marcellus shale is quartz-rich, containing more than 70% quartz. The Longmaxi shale also has a relatively high amount of quartz at nearly 50%, with an addition of 20% calcite. The chemical compositions were used to estimate the effective scattering length density (SLD) of each shale sample. We can see that sample with a relatively high TOC content has a relatively low estimated effective SLD. The estimated SLDs were used for SANS data analysis to characterize the information of nanopore structures quantitatively.

2.2 Contrast-matching SANS measurement

The contrast-matching SANS measurements were conducted using the vSANS instrument at the NIST Center for Neutron Research (NCNR). Each dried powder sample was filled into an aluminum capsule, and then the aluminum capsule was placed into the high-pressure cell as shown in Fig. S1. The neutron wavelength λ was set at 6 Å. A small λ helps to minimize the multiple scattering effect. The neutron wavelength spread Δλ/λ was 0.12. Two configurations were used for the measurements. The first configuration named as NG7 using the sample-to-detector distances of 1.93 m for the Front four detectors and of 9.13 m for the Middle four detectors to cover a scattering vector Q range between ~4.8×10^{-3} and ~0.34 $Å^{-1}$, corresponding to a length scale d, or pore diameter, range between ~1.3×10^{3} and ~18.6 Å, where the relationship $d = 2\pi/Q$ was used.

The second configuration named as NG2 using the sample-to-detector distances of 4.13 m for the Front four detectors and of 19.13 m for the Middle four detectors to cover a Q range between ~2.5×10^{-3} and ~0.16 $Å^{-1}$, corresponding to a d range between ~2.5×10^{3} and ~38.6 Å. Both the NG7 and NG2 configurations were used to measure the Marcellus shale and Longmaxi shale samples. Only the NG7 configuration was used to measure the Illinois shale sample due to limited beam time.

All three shale samples were dosed by deuterated methane (CD_4) with incremental gas pressure for the contrast-matching SANS measurements. The maximum conducting pressure was 700 bar for the Marcellus shale and the Longmaxi shale samples and 600 bar for the Illinois shale sample. Scattering counts were measured under vacuum condition first and then under each incremental pressure with 100 bar as the pressure interval till the maximum conducting pressure for each sample. Scattering counts were measured under vacuum condition again after the methane injection for all the samples. After the data acquisition, obtained 2D scattering profiles were radially averaged to 1D scattering profiles for each configuration using the Igor macros vSANS procedures [38]. 1D scattering profiles at two sample-to-detector distances were merged for each configuration. For the Marcellus shale and Longmaxi shale samples using two configurations during the measurements, 1D scattering profiles of the two configurations were further merged.

3. Results and discussion

In this section, we first provide the interpretation of SANS data analyses and pore structure information of the measured shale samples as baseline information. Then, we estimate the average SLDs in the accessible pores, which will give the information of gas condensation under confinement and gas storage mechanisms. At last, we provide the implication of gas storage in underground shale reservoirs.

3.1 SANS data analyses and pore structures of the measured shales

The background-subtracted scattering intensities as a function of Q and methane pressure for the Marcellus shale are shown in Fig. 1, and for the Illinois shale and Longmaxi shale samples are shown in Figs. S2 and S4 in the Supporting Information (SI). The flat scattering background was estimated by fitting the scattering intensity in the Q range from 0.3 $Å^{-1}$ to the highest Q value for each shale sample's scattering profile. We can see that scattering intensity decreases with increasing pressure at middle and low Q regions. However, scattering intensities do not have noticeable change and have higher uncertainties at the high Q region. By choosing specific Q values at the middle, low, and high Q regions, scattering intensity at each Q value as a function of pressure can be demonstrated in detail, and the data can be compared (Figs. 2, S3, and S5). Scattering intensity at the representative middle or low Q value rapidly decreases as gas pressure increases and gradually decreases with further increasing pressure for all the samples (Figs. 2ab, S3ab, and S5ab). This is because the increase of SLD of CD_4 as a function of gas pressure is known to be nonlinear, as shown in Table S1 and Fig. S6 in the SI. SLD of CD_4 rapidly increases with increasing pressure before 300 bar, followed by a gentle and gradual increase of SLD after 300 bar. However, there is no clear trend between scattering intensity and gas pressure at the representative high Q value for each sample (Figs. 2c, S3c, and S5c), indicating either CD_4 is already highly densified at small nanopores before 100 bar or limited fine pores are accessible to the guest gas or incoherent background has already surpassed the elastic intensity of fine pores which was subtracted initially [39]. We can tell that the Marcellus shale sample has reached the contrast-matched condition at ~ 600 bar at low Q and ~ 400 bar at middle Q (Fig. 1ab). However, the Illinois shale and Longmaxi shale samples did not reach the contrast-matched point experimentally but were approaching (Figs. S3ab and S5ab). Reaching the contrast-matched point

at a smaller pressure at the middle Q region compared to the low Q region indicates a smaller SLD of the solid matrix surrounding middle-sized pores than large-sized pores for the Marcellus shale sample. Since most mineral matter have higher SLD than organic carbon, organic matter in Marcellus shale could contain smaller pores than mineral matter [9, 40]. Another possible reason could be a higher degree of gas densification in smaller pores [32, 39].

Pore accessibilities of three shale samples were estimated by the previously determined method using the scattering intensities under vacuum and contrast-matched conditions [41, 42]

$$C_{\mathrm{ac}}(Q) = 1 - \frac{I_{\mathrm{cm}}(Q)}{I_{\mathrm{va}}(Q)} \qquad (1)$$

where $I_{\mathrm{va}}(Q)$ and $I_{\mathrm{cm}}(Q)$ are the background-subtracted scattering intensities under vacuum and contrast-matched conditions, respectively. Since we used powder samples, the estimated pore accessibility should be the volumetric and statistical average pore accessibility of each shale sample [40], where the results are shown in Fig. 3a. We can find that pore accessibilities of the three shale samples decrease with increasing Q in general, which provides direct evidence that the smaller pore is less accessible. Pore accessibilities of the Marcellus shale and Longmaxi shale samples are higher than that of Illinois shale, which could be because of lower amounts of organic matter in the Marcellus shale and Longmaxi shale samples in comparison with Illinois shale. The Longmaxi shale has the smallest TOC and has the highest pore accessibility among the measured samples.

Furthermore, pore volume distributions of the shale samples were estimated by the model fitting method [39, 40, 43]. The background-subtracted 1D scattering profiles under vacuum condition were used to fit using the maximum entropy (MaxEnt) method in the Igor macros Irena package [44]. Without using a statistic function of pore size distribution, the MaxEnt method can provide a

more accurate result in multimodal pore volume distribution for a given two-phase porous material. The background-subtracted scattering intensity can be expressed as [45]

$$I(Q) = N\left(\rho_{\mathrm{s}}^{*} - \rho_{\mathrm{p}}^{*}\right)^{2} \int V^{2}(r) f(r) P(Q,r) dr \qquad (2)$$

where N is the pore number density; ρ_{s}^{*} and ρ_{p}^{*} are the SLDs of the solid matrix and the pores; r is the spherical radius; $V(r)$ is the spherical volume; $f(r)$ is the pore size distribution; and $P(Q,r)$ is the spherical form factor. SLD of the pores (ρ_{p}^{*}) should be zero under vacuum condition. The estimated effective SLD of each shale sample in Table S2 was used for the solid matrix SLD. The upper and lower limits of the pore diameter were set as 3000 Å and 10 Å for the model-fitting of the Marcellus shale and Longmaxi shale samples. However, for the Illinois shale sample, a smaller upper limit of the pore diameter (1500 Å) was used because only the NG7 configuration was used for the measurement due to the limited beam time. Thus, the probed pore diameter size range is 1-300 nm for Marcellus and Longmaxi shale sample and 1-150 nm for the Illinois shale. The results of pore volume distributions with uncertainties are shown in Fig. 3b. The unit of volume distribution is $cm^3/(cm^3*Å)$ i.e., dV/(V*dD). We can find that pore volume distributions of all the shale samples are multimodal. The main peak at the pore diameter of ~20 Å and a small peak at the pore diameter of ~55 Å are shown in the volume distributions of the Marcellus shale and Illinois shale samples. However, a relatively lower and broader hump at the pore range around 20-300 Å is shown in the volume distribution of the Longmaxi shale sample. We can see multiple peaks at larger pores ranging between 100 Å and 1000 Å for the Illinois shale sample, in which the volume distribution is higher than the other two shale samples due to the relatively more pore population in larger sized pores. The Marcellus and Longmaxi shale samples have very similar pore volume distributions at pore diameter greater than ~100 Å, and both have small hump at pores around 1500 Å.

Besides, cumulative porosities and surface areas of the three samples were estimated based on the estimated pore volume distributions. The cumulative porosity and surface area can be estimated as [43, 44]

$$\emptyset = N \int f(r)V(r)dr \qquad (3)$$

$$S = N \int f(r)A(r)dr \qquad (4)$$

where $A(r)$ is the spherical surface area. The results of cumulative porosities and surface areas are shown in Fig. 3c and d. There is a three-stage porosity increase with increasing pore size for the Marcellus shale and Illinois shale samples and a two-stage increase of porosity for the Longmaxi shale sample as shown in Fig. 3c. A rapid increase at the pore diameter around 30 Å for the Marcellus shale and Illinois shale samples is because of the major peak of volume distribution (Fig. 3b). And then, porosity gradually increases till ~150 Å for the Illinois shale sample and till ~1000 Å for the Marcellus shale sample. After that, porosity rapidly increases till the upper pore limit, that the SANS instrument can measure, for these two samples. In contrast, the Longmaxi shale sample has a moderate increase of porosity before 1000 Å and a rapid increase of porosity after 1000 Å. Overall, the Illinois shale sample has a much higher total porosity than the other two shale samples at the pore size of 1500 Å, which is the maximum measured pore size of the Illinois shale sample. The surface area rapidly increases at the pore around 250 Å and gradually increases further for the Illinois shale sample. The surface area of the Marcellus shale sample also rapidly increases at the pore with a size of ~250 Å but barely increases afterward. The Longmaxi shale sample seems to have a gradual increase of surface area over the entire pore range.

To characterize the nanopore structure evolution under different pressure conditions for the shale samples, we have applied a global scattering function integrated Guinier approximation and power-law scattering, a unified scattering model, for data-fitting, in which the unified scattering

model is superior to differentiate multiple structures in multiscale in a hierarchical porous medium. The method has been successfully used in shale in previous studies [25, 46]. The unified scattering equation to describe multiple interrelated structural levels over a broad range of Q without considering background can be expressed as [47]

$$I(Q) = \sum_{i=1}^{n}[G_i \exp(-Q^2 R_{g\,i}^2/3) + B_i \exp(-Q^2 R_{g\,i+1}^2/3) \times (Q^*)^{-P_i}] \quad (5)$$

$$Q^* = Q\left[\mathrm{erf}\left(QR_{g\,i}/\sqrt{6}\right)\right]^{-3} \quad (6)$$

where the first term in Eq. 5 is the Guinier's exponential form and the second term is the structurally limited power-law form. Q^* is the modified scattering vector Q containing a three-dimensional Gaussian probability function, which accounts for the finite structural effect in the power-law region. G is the classic Guinier prefactor; R_g is the radius of gyration describing the domain size; B is the power-law prefactor; P is the power-law exponent; and i is the structural level, in which $i = 1$ refers to the largest-size structural level. The fitting of each scattering profile was conducted using SasView [48]. The representative model fitting profiles can be found in Fig. S7, and the fitting parameters can be found in Figs. S8-S9 and Table S3-S5. A detailed discussion can be found in the SI.

3.2 The average SLD in open pores

We have used the bulk phase SLD of the injected gases to estimate the changes of pore volume and surface area with increased gas pressure in our previous studies [39, 43]. The method ignores the contribution of the SLD of adsorbed phase density in pores. To characterize the average SLD or average density fluctuation in pores under elevated pressure conditions for the shale samples, the structure-free Porod invariant method considering three-phase approximation (*i.e.,* solid matrix, open pores, and closed pores, as shown in Fig. 4) can be used. The three-phase Porod invariant equation may be expressed as

$$Q_{\mathrm{inv}} = \int_{Q_{\mathrm{min}}}^{Q_{\mathrm{max}}} Q^2 I(Q) dQ = 2\pi^2[(\rho_{\mathrm{s}}^* - \rho_{\mathrm{o}}^*)^2 \emptyset_{\mathrm{s}} \emptyset_{\mathrm{o}} + (\rho_{\mathrm{s}}^* - \rho_{\mathrm{c}}^*)^2 \emptyset_{\mathrm{s}} \emptyset_{\mathrm{c}} + (\rho_{\mathrm{o}}^* - \rho_{\mathrm{c}}^*)^2 \emptyset_{\mathrm{o}} \emptyset_{\mathrm{c}}] \quad (7)$$

$$\emptyset_{\mathrm{s}} + \emptyset_{\mathrm{o}} + \emptyset_{\mathrm{c}} = 1 \quad (8)$$

where Q_{max} and Q_{min} are the maximum and minimum Q, which can be measured by the configuration of SANS experiments; ρ_{o}^* and ρ_{c}^* are the SLDs of the open and closed pores, respectively; and $\emptyset_{\mathrm{s}}$, $\emptyset_{\mathrm{o}}$, and $\emptyset_{\mathrm{c}}$ are the volume fractions of the solid matrix, open pores, and closed pores, respectively. Q_{inv} can be estimated using the experimentally obtained scattering intensity under different pressure conditions, which is shown in Fig. 5. Note that the Q range to estimate the Porod invariant was set as 2.8×10^{-3} - 0.25 $Å^{-1}$, 5.3×10^{-3} - 0.25 $Å^{-1}$, and 2.5×10^{-3} - 0.21 $Å^{-1}$ for the Marcellus shale, Illinois shale, and Longmaxi shale samples, respectively. Then the results can be more precisely compared among different pressure conditions for each sample, although some portion of high Q was ignored. The Marcellus shale sample may already reach the contrast-matched point at the pressure around 600 bar on average over the estimated pore range (Fig. 5). The SLD of CD_4 at 600 bar in room temperature is about 3.7×10^{10} cm^{-2}, which is slightly smaller than the estimated effective SLD (~3.9×10^{10} cm^{-2}) from the chemical compositions of the Marcellus shale. It suggests that slightly more open nanopores accessible to CD_4 are in the matrix with a smaller SLD, which could be organic matter. In contrast, the Longmaxi shale sample may approach the contrast-matched point at the pressure around 700 bar, and the Illinois shale sample may not reach the contrast-matched point over the pressure range measured (Fig. 5). It is unexpected for the two samples because the estimated effective SLD of the Longmaxi shale sample (~4.4×10^{10} cm^{-2}) is higher than the SLD of CD_4 at the highest pressure (700 bar), which is ~3.9×10^{10} cm^{-2}, and the estimated effective SLD of the Illinois shale sample (~3.4×10^{10} cm^{-2}) is less than the SLD of CD_4 at the pressure of 600 bar (~3.7×10^{10} cm^{-2}). The results suggest that more open nanopores accessible to CD_4 are in the Longmaxi shale sample matrix with a lower SLD,

278 which could be organic matter, while in the matrix of the Illinois shale sample with a higher SLD,
279 which could be clay minerals such as glauconite.

280 In order to estimate the average SLD in open pores, ρ_o^*, using Eq. 7, the volume fractions
281 of the solid matrix, open pores, and closed pores, $\emptyset_s$, $\emptyset_o$, and $\emptyset_c$, need to be quantified. The
282 average SLD in closed pores, ρ_c^* is equal to zero since the guest fluid does not have access to closed
283 pores, and there may be no residual fluid inside closed pores. ρ_o^* is equal to zero under vacuum
284 condition because of empty pores and equal to ρ_s^* under contrast-matched condition. Thus, in both
285 conditions, the three-phase Porod invariant equation reduces to the two-phase one

286 $$\text{Vacuum: } Q_{\text{inv}} = \int_{Q_{\min}}^{Q_{\max}} Q^2 I(Q) dQ = 2\pi^2 (\rho_s^*)^2 \emptyset_s (\emptyset_o + \emptyset_c) \quad (9)$$

287 $$\text{Contrast-matched: } Q_{\text{inv}} = \int_{Q_{\min}}^{Q_{\max}} Q^2 I(Q) dQ = 2\pi^2 (\rho_s^*)^2 (\emptyset_s + \emptyset_o) \emptyset_c \quad (10)$$

288 where the volume fraction of total pores equals to $\emptyset_o + \emptyset_c$. Since ~600 bar could be the contrast-
289 matched pressure of the Marcellus shale sample, the SLD of CD_4 at 600 bar (3.7×10^{10} cm^{-2}) was
290 used as the SLD of the sample along with the Q_{inv} at that pressure to quantify volume fractions of
291 total and closed pores and the average SLD in open pores in the Marcellus shale sample. However,
292 parabolic curve-fitting using the last five data points may give the smallest Q_{inv} and the contrast-
293 matched pressure for the Illinois shale and Longmaxi shale samples. The estimated Q_{inv} and
294 pressure at the contrast-matched point could be 1.33×10^{-3} $cm^{-1}Å^{-3}$ and 711 bar for the Illinois shale
295 sample and 3.40×10^{-4} $cm^{-1}Å^{-3}$ and 618 bar for the Longmaxi shale sample. The approximate
296 contrast-matched SLD can be obtained, which is 3.90×10^{10} cm^{-2} for the Illinois shale sample and
297 3.73×10^{10} cm^{-2} for the Longmaxi shale sample. The estimated contrast-matched SLDs were used
298 to estimate the volume fractions of total and closed pores and the average SLD in open pores.
299 Table S6 shows the estimated volume fractions of open and closed pores and the corresponding
300 average pore accessibility. We can find that the Longmaxi shale sample has the highest volume

fraction of open pores. However, the Illinois shale sample has the highest volume fraction of closed pores, as expected, because of the highest amount of organic matter among the three shale samples. Accordingly, the Illinois shale sample has the smallest pore accessibility on average, consistent with the size-dependent result shown in Fig. 3a. Besides, Pearson correlation analysis was conducted using the variables of TOC, maturity, contrast-matched SLD, the volume fraction of total pores, and pore accessibility. The correlation coefficients are shown in Table S7. We can find that TOC and total pores are positively correlated. A highly negative correlation is shown between TOC and pore accessibility. However, since we have only measured three shale samples, those correlations may be different using more samples with diverse mineral and organic components, and thus further study will be needed.

Using the estimated volume fractions of open and closed pores and the contrast-matched SLDs, the average SLD in open pores over the specified pore range as a function of pressure for each sample can be quantified, as shown in Fig. 6. Here the assumption is that the volume fractions of open and closed pores do not change under pressurized conditions, which may hold for shale rocks. The SLD of bulk CD_4 as a function of pressure is also shown in the figure for comparison. Note that the Q range for estimation of the average SLD in pores was set as 2.8×10^{-3} - 0.25 $Å^{-1}$, 5.3×10^{-3} - 0.25 $Å^{-1}$, and 2.5×10^{-3} - 0.21 $Å^{-1}$ for the Marcellus shale, Illinois shale, and Longmaxi shale samples, respectively. By using the relationship $d = 2\pi/Q$, the pore diameter range is 2.3×10^{3} - 25 Å, 1.2×10^{3} - 25 Å, and 2.5×10^{3} - 30 Å for the Marcellus shale, Illinois shale, and Longmaxi shale samples, respectively. We can find that the average SLDs of the three samples over the quantified pore range are smaller than that of bulk CD_4 when the pressure is smaller than the contrast-matched pressure of each sample except for the SLDs at the pressure of 100 bar for the Marcellus shale and Illinois shale samples (Fig. 6). When the pressure is higher than the

contrast-matched pressure, the average SLD in pores becomes greater than the SLD of the bulk phase for the Marcellus shale and Longmaxi shale samples. It is well known that the stored gas in shale nanopores could include both bulk gas and adsorbed gas. The average SLD in open pores may be expressed as

$$\rho_{\mathrm{ave}}^{*} = \emptyset_{\mathrm{b}}\rho_{\mathrm{b}}^{*} + \emptyset_{\mathrm{a}}\rho_{\mathrm{a}}^{*} \qquad (11)$$

where ρ_{b}^{*} and ρ_{a}^{*} are the SLDs of the bulk phase and adsorbed phase, respectively; and $\emptyset_{\mathrm{b}}$ and $\emptyset_{\mathrm{a}}$ are the volume fractions of the bulk phase and adsorbed phase, respectively, in which the sum of $\emptyset_{\mathrm{b}}$ and $\emptyset_{\mathrm{a}}$ is equal to one. A higher ρ_{ave}^{*} than ρ_{b}^{*} suggests a higher ρ_{a}^{*} than ρ_{b}^{*} on average in the integrated pore range, *vice versa*. The measured samples' results hypothetically indicate that the adsorbed phase density, ρ_{a}, in shale macro-/mesopores on average could be higher than the bulk phase density, ρ_{b}, at the low-pressure region (< ~100 bar) because of surface adsorption (Fig. 7). However, the average ρ_{a} could become smaller than the ρ_{b} at a higher pressure because of the increase of adsorbed phase volume, V_{a}, in which surface adsorption could convert to partial pore-filling adsorption (Fig. 7). When the gas pressure is even higher, there could be two situations: (1) the completion of pore-filling adsorption occurs, in which the V_{a} increased to be the pore volume; (2) the decrease of V_{a} occurs (Fig. 7). The second situation may be more likely in shale macro-/mesopores because these nanopores may not have enough overlapped energy from the pore surface to provide a possible complete pore-filling adsorption. From a laboratory perspective, the excess or Gibbs adsorption capacity can be directly estimated either by gravimetric or volumetric methods [49]. In contrast, the absolute adsorption capacity, representing the real adsorption capability, can only be estimated by correcting the excess adsorption capacity through assumptions. The usual assumption of constant adsorbed phase density [13, 16] could have less error in relatively low pressure than higher pressure regions. The assumption of monolayer sorption volume or pore volume as

347 constant adsorbed phase volume [50, 51] could have higher errors for sorption capacity estimation.
348 However, since we only measured three shale samples and do not have data points at relatively
349 low-pressure (< 100 bar) and significantly high-pressure regions (> 700 bar) because of limited
350 beam time, further research, either experimental or computational approaches, need to be
351 conducted to prove the hypothetical mechanism.

352 In addition, we have used three separated Q ranges for the Marcellus and Longmaxi shale
353 samples and two separated Q ranges for the Illinois shale sample to estimated Porod invariants as
354 a function of pressure using Eq. 7 as shown in Fig. S10 and further estimate the average SLDs in
355 open pores as shown in Fig. S11. The approximate segmentation is based on the definition of
356 meso-/macropores. The determined contrast-matched pressures and corresponding SLDs are
357 shown in Table S8. We can see that mesopores have a lower average SLD than macropores for all
358 the samples when pressure is higher than 100 bar, indicating a smaller average adsorbed phase
359 density in mesopores. A possible reason could be that occupation of gas molecules or adsorbed
360 phase volume at low pressure (< 100 bar) in mesopores is relatively higher than macropores. When
361 pressure continuously increases, lesser gas molecules could be adsorbed in mesopores, in which
362 the average adsorbed phase density will be smaller in mesopores.

363 **3.3 The implication on methane storage and CO_2 sequestration in shale reservoirs**

364 For carbon storage or sequestration in subsurface formations, all the potential phases,
365 including bulk phase, chemically reacted phase(s), physically adsorbed phase, and even dissolved
366 phase(s), will contribute to the total gas storage or sequestration in shale reservoirs. In this study,
367 since we used a single-phase dry gas, the stored phases could only be the bulk and adsorbed phases.
368 From the previous section, the average SLDs in nanopores under different pressure conditions

were quantified. The gas density and SLD of CD_4 have an approximately linear correlation shown in Table S2. The total gas storage in shale nanopores may be estimated by

$$m = \rho_{\mathrm{ave}} V_{\mathrm{o}}/m_{\mathrm{s}} = \rho_{\mathrm{ave}}[(V_{\mathrm{o}}/V_{\mathrm{t}})/(V_{\mathrm{s}}/V_{\mathrm{t}})]/(m_{\mathrm{s}}/V_{\mathrm{s}}) \cong \rho_{\mathrm{ave}}(\emptyset_{\mathrm{o}}/\emptyset_{\mathrm{s}})/\rho_{\mathrm{he}} \quad (12)$$

where ρ_{ave} is the average gas density in pores; V_{o}, V_{s}, and V_{t} are the volumes of open pores, solid matrix, and total matrix, respectively; m_{s} is the mass of the solid matrix; ρ_{he} is the helium density; and m is the total gas storage capacity per unit mass. The helium densities of 2.55 g/cm^3, 2.07 g/cm^3, and 2.72 g/cm^3 was used for the Marcellus shale, Illinois shale, and Longmaxi shale samples, respectively. The estimated methane storage capacities as a function of pressure for the measured three shale samples are shown in Fig. 8. The excess adsorption capacities of the shale samples are also shown for comparison, although they were measured in the low-pressure region. Detailed information on the experimental operation and adsorption capacity estimation can be found in paper [15], and a schematic of the experimental system is shown in Fig. S12. All the volumetric adsorption capacities are higher than the methane storage capacities obtained by *in situ* SANS at the low-pressure region for the samples (Fig. 8). One possible reason could be that pores with overall sizes contribute to the volumetric adsorption, while only a limited pore range was used to estimate methane storage capacity from *in situ* SANS data. As mentioned in the previous section, the pore diameter range for the estimation is 2.3×10^3 - 25 Å for the Marcellus shale sample, 1.2×10^3 - 25 Å for the Illinois shale sample, and 2.5×10^3 - 30 Å for the Longmaxi shale sample. We can see that the micropore region was excluded entirely in the estimation because the measured high Q limit of the SANS profiles is not high enough to reach the length scale of micropores. Even though the high Q limit is high enough to access the length scale of micropores, the scattering background could be higher than the scattering of micropores restricting the micropore information to be quantified. If we assume most of the volumetric adsorption capacity is the gas storage in

micropores because of high specific surface area [11], we can see the micropore gas storage at the pressure of ~100 bar is as high as the total gas storage in macro-/mesopores at the pressure of ~600 bar for the Illinois shale (blue curves in Fig. 8). The sample is highly organic-rich with a TOC of ~30%. The storage capacity in adsorption in micropores is approximately four times higher than the storage capacity of both bulk and adsorbed gas in macro-/mesopores at the pressure of ~100 bar. We may conclude that adsorption could dominate total gas storage in nanopores at relatively low pressure in a highly organic-rich shale sample. For the relatively less organic-rich shale samples, *i.e.*, Marcellus shale and Longmaxi shale samples, the gas adsorption in micropores is less dominant than the total gas storage in the low-pressure region (red and yellow curves in Fig. 8). At the pressure of 200 bar, the total gas capacity is slightly higher than the adsorption one for the Longmaxi shale sample. The total gas capacity is very similar to the adsorption one at the pressure of 300 bar for the Marcellus shale sample. It is interesting to find that the adsorption capacity has a positive correlation with TOC, and the total gas storage capacity at the pressure of 100 bar also has a positive correlation with TOC, although only three shale samples were measured here. The total gas storage capacity at the pressures of 200 bar and 300 bar are similar among these samples. When the pressure is beyond 300 bar, Longmaxi shale with the highest open pores has the highest total gas storage capacity. The results suggest that a target shale reservoir with a high gas storage capacity either for methane storage or CO_2 sequestration could depend on three essential factors: the final equilibrium pressure, TOC, and the accessible porosity. TOC seems like only affecting the gas storage capacity at relatively low pressure. However, other factors such as geological fault, reservoir depth, and cap rocks quality will be considered for gas storage security in the long term. Indeed, the gas injection rate will depend on intrinsic permeability and diffusion in fractures and pores in complex shale.

4. Conclusions

This study provides an investigation of high-pressure gas storage mechanisms of three shale samples using *in situ* SANS measurements with contrast-matching method. From basic characterization, the Marcellus sahale and Longmaxi shale samples are qurtz-rich and the Illinois shale sample has the highest TOC. The Marcellus sahale and Longmaxi shale samples have higher pore accessibility than the Illinois shale sample. However, the Illinois shale has the highest cumulative porosity and surface area among the measured samples.

Based on the three-phase Porod invariant method, the average SLD in accessible pores of the measured shale samples can be obtained. The results indicate a lower average adsorbed phase density in accessible pores of shale than bulk phase density at the pressure between 100 bar and the contrast-matched point (~600-700 bar). In contrast, the average adsorbed phase density could be higher than bulk when the pressure is below 100 bar and above the contrast-matched pressure. Hyphohetically, the average adsorbed phase volume could first increase and then decrease with increasing pressure till very high-pressure region. However, further study needs to be conducted at low pressure and very high-pressure regions to confirm these mechanisms and more samples also need to be considered.

In addition, gas storage capacities of the shales were estimated. The results are compared with the previously measured gas adsorption capacities of the same shale samples. TOC has positive correlation with both the gas adsorption capacity and storage capacity at low pressure. Longmaxi shale with the highest pore accessibility has the highest gas storage capacity at high pressure. Therefore, three essential factors, including the final injection pressure, TOC, and the accessible porosity, could be used for searching and maximizing methane storage and long-term CO_2 sequestration in depleted shale reservoir.

References

1. EIA, *Annual Energy Outlook 2020: With Projections to 2050*, Government Printing Office, 2020.
2. R. W. Howarth, A. Ingraffea and T. Engelder, Natural gas: Should fracking stop?, *Nature*, 2011, **477**, 271-275.
3. R. A. Kerr, Natural Gas From Shale Bursts Onto the Scene, *Science*, 2010, **328**, 1624-1626.
4. L. Cueto-Felgueroso and R. Juanes, Forecasting long-term gas production from shale, *Proceedings of the National Academy of Sciences of the United States of America*, 2013, **110**, 19660-19661.
5. V. Masson-Delmotte, P. Zhai, H.-O. Pörtner, D. Roberts, J. Skea, P. R. Shukla, A. Pirani, W. Moufouma-Okia, C. Péan and R. Pidcock, Global warming of 1.5 C, *An IPCC Special Report on the impacts of global warming of*, 2018, **1**.
6. E. National Academies of Sciences and Medicine, *Negative emissions technologies and reliable sequestration: a research agenda*, National Academies Press, 2019.
7. C. Bousige, C. M. Ghimbeu, C. Vix-Guterl, A. E. Pomerantz, A. Suleimenova, G. Vaughan, G. Garbarino, M. Feygenson, C. Wildgruber, F. J. Ulm, R. J. M. Pellenq and B. Coasne, Realistic molecular model of kerogen's nanostructure, *Nature Materials*, 2016, **15**, 576-+.
8. G. R. Chalmers, R. M. Bustin and I. M. Power, Characterization of gas shale pore systems by porosimetry, pycnometry, surface area, and field emission scanning electron microscopy/transmission electron microscopy image analyses: Examples from the Barnett, Woodford, Haynesville, Marcellus, and Doig units, *Aapg Bulletin*, 2012, **96**, 1099-1119.
9. X. Gu, D. R. Cole, G. Rother, D. F. R. Mildner and S. L. Brantley, Pores in Marcellus Shale: A Neutron Scattering and FIB-SEM Study, *Energy & Fuels*, 2015, **29**, 1295-1308.
10. C. R. Clarkson, N. Solano, R. M. Bustin, A. M. M. Bustin, G. R. L. Chalmers, L. He, Y. B. Melnichenko, A. P. Radlinski and T. P. Blach, Pore structure characterization of North American shale gas reservoirs using USANS/SANS, gas adsorption, and mercury intrusion, *Fuel*, 2013, **103**, 606-616.
11. Y. Wang, Y. Zhu, S. Liu and R. Zhang, Pore characterization and its impact on methane adsorption capacity for organic-rich marine shales, *Fuel*, 2016, **181**, 227-237.
12. T. F. Rexer, E. J. Mathia, A. C. Aplin and K. M. Thomas, High-Pressure Methane Adsorption and Characterization of Pores in Posidonia Shales and Isolated Kerogens, *Energy & Fuels*, 2014, **28**, 2886-2901.
13. Y. Wang, Y. M. Zhu, S. M. Liu and R. Zhang, Methane adsorption measurements and modeling for organic-rich marine shale samples, *Fuel*, 2016, **172**, 301-309.
14. R. Heller and M. Zoback, Adsorption of methane and carbon dioxide on gas shale and pure mineral samples, *Journal of Unconventional Oil and Gas Resources*, 2014, **8**, 14-24.
15. L. Fan and S. Liu, A novel experimental system for accurate gas sorption and its application to various shale rocks, *Chemical Engineering Research and Design*, 2021, **165**, 180-191.
16. M. Gasparik, A. Ghanizadeh, P. Bertier, Y. Gensterblum, S. Bouw and B. M. Krooss, High-Pressure Methane Sorption Isotherms of Black Shales from The Netherlands, *Energy & Fuels*, 2012, **26**, 4995-5004.
17. H. Tian, T. F. Li, T. W. Zhang and X. M. Xiao, Characterization of methane adsorption on overmature Lower Silurian-Upper Ordovician shales in Sichuan Basin, southwest China: Experimental results and geological implications, *International Journal of Coal Geology*, 2016, **156**, 36-49.

18. Y. X. Ma and A. Jamili, Modeling the density profiles and adsorption of pure and mixture hydrocarbons in shales, *Journal of Unconventional Oil and Gas Resources*, 2016, **14**, 128-138.
19. K. Mosher, J. He, Y. Liu, E. Rupp and J. Wilcox, Molecular simulation of methane adsorption in micro- and mesoporous carbons with applications to coal and gas shale systems, *International Journal of Coal Geology*, 2013, **109**, 36-44.
20. J. Berthonneau, A. Obliger, P. L. Valdenaire, O. Grauby, D. Ferry, D. Chaudanson, P. Levitz, J. J. Kim, F. J. Ulm and R. J. M. Pellenq, Mesoscale structure, mechanics, and transport properties of source rocks' organic pore networks, *Proceedings of the National Academy of Sciences of the United States of America*, 2018, **115**, 12365-12370.
21. S. Fuss, J. G. Canadell, G. P. Peters, M. Tavoni, R. M. Andrew, P. Ciais, R. B. Jackson, C. D. Jones, F. Kraxner, N. Nakicenovic, C. Le Quéré, M. R. Raupach, A. Sharifi, P. Smith and Y. Yamagata, Betting on negative emissions, *Nat Clim Change*, 2014, **4**, 850-853.
22. L. M. Anovitz and D. R. Cole, in *Pore-Scale Geochemical Processes*, eds. C. I. Steefel, S. Emmanuel and L. M. Anovitz, 2015, vol. 80, pp. 61-164.
23. L. M. Anovitz and D. R. Cole, Analysis of the Pore Structures of Shale Using Neutron and X‐Ray Small Angle Scattering, *Geological Carbon Storage*, 2019, 71-118.
24. J. Bahadur, Y. B. Melnichenko, M. Mastalerz, A. Furmann and C. R. Clarkson, Hierarchical Pore Morphology of Cretaceous Shale: A Small-Angle Neutron Scattering and Ultrasmall-Angle Neutron Scattering Study, *Energy & Fuels*, 2014, **28**, 6336-6344.
25. S. Lee, T. B. Fischer, M. R. Stokes, R. J. Klingler, J. Ilavsky, D. K. McCarty, M. O. Wigand, A. Derkowski and R. E. Winans, Dehydration effect on the pore size, porosity, and fractal parameters of shale rocks: Ultrasmall-angle X-ray scattering study, *Energy & Fuels*, 2014, **28**, 6772-6779.
26. M. D. Sun, B. S. Yu, Q. H. Hu, Y. F. Zhang, B. Li, R. Yang, Y. B. Melnichenko and G. Cheng, Pore characteristics of Longmaxi shale gas reservoir in the Northwest of Guizhou, China: Investigations using small-angle neutron scattering (SANS), helium pycnometry, and gas sorption isotherm, *International Journal of Coal Geology*, 2017, **171**, 61-68.
27. H. E. King, A. P. R. Eberle, C. C. Walters, C. E. Kliewer, D. Ertas and C. Huynh, Pore Architecture and Connectivity in Gas Shale, *Energy & Fuels*, 2015, **29**, 1375-1390.
28. L. F. Ruppert, R. Sakurovs, T. P. Blach, L. He, Y. B. Melnichenko, D. F. R. Mildner and L. Alcantar-Lopez, A USANS/SANS study of the accessibility of pores in the Barnett shale to methane and water, *Energy & Fuels*, 2013, **27**, 772-779.
29. X. Gu, D. F. R. Mildner, D. R. Cole, G. Rother, R. Slingerland and S. L. Brantley, Quantification of Organic Porosity and Water Accessibility in Marcellus Shale Using Neutron Scattering, *Energy & Fuels*, 2016, **30**, 4438-4449.
30. J. Bahadur, L. F. Ruppert, V. Pipich, R. Sakurovs and Y. B. Melnichenko, Porosity of the Marcellus Shale: A contrast matching small-angle neutron scattering study, *International Journal of Coal Geology*, 2018, **188**, 156-164.
31. K. L. Stefanopoulos, T. G. A. Youngs, R. Sakurovs, L. F. Ruppert, J. Bahadur and Y. B. Melnichenko, Neutron Scattering Measurements of Carbon Dioxide Adsorption in Pores within the Marcellus Shale: Implications for Sequestration, *Environmental Science & Technology*, 2017, **51**, 6515-6521.
32. A. P. R. Eberle, H. E. King, P. I. Ravikovitch, C. C. Walters, G. Rother and D. J. Wesolowski, Direct Measure of the Dense Methane Phase in Gas Shale Organic Porosity by Neutron Scattering, *Energy & Fuels*, 2016, **30**, 9022-9027.

33. Y. B. Melnichenko, *Small-Angle Scattering from Confined and Interfacial Fluids: Applications to Energy Storage and Environmental Science*, Springer International Publishing, 2015.
34. D. Kohl, R. Slingerland, M. Arthur, R. Bracht and T. Engelder, Sequence stratigraphy and depositional environments of the Shamokin (Union Springs) Member, Marcellus Formation, and associated strata in the middle Appalachian Basin, *Aapg Bulletin*, 2014, **98**, 483-513.
35. R. H. Shaver, *Compendium of Paleozoic rock-unit stratigraphy in Indiana: A revision*, Department of Natural Resources, 1986.
36. C. E. Wier, *Geology and mineral deposits of the Jasonville Quadrangle, Indiana*, Indiana Geological Survey, 1952.
37. C. Zou, D. Dong, S. Wang, J. Li, X. Li, Y. Wang, D. Li and K. Cheng, Geological characteristics and resource potential of shale gas in China, *Petroleum Exploration and Development*, 2010, **37**, 641-653.
38. S. Kline, Reduction and analysis of SANS and USANS data using IGOR Pro, *Journal of Applied Crystallography*, 2006, **39**, 895-900.
39. S. M. Liu, R. Zhang, Z. Karpyn, H. Yoon and T. Dewers, Investigation of accessible pore structure evolution under pressurization and adsorption for coal and shale using small-angle neutron scattering, *Energy & Fuels*, 2019, **33**, 837-847.
40. R. Zhang, S. Liu, L. He, T. P. Blach and Y. Wang, Characterizing anisotropic pore structure and its impact on gas storage and transport in coalbed methane and shale gas reservoirs, *Energy & Fuels*, 2020, **34**, 3161-3172.
41. Y. B. Melnichenko, L. He, R. Sakurovs, A. L. Kholodenko, T. Blach, M. Mastalerz, A. P. Radlinski, G. Cheng and D. F. R. Mildner, Accessibility of pores in coal to methane and carbon dioxide, *Fuel*, 2012, **91**, 200-208.
42. R. Zhang, S. Liu, J. Bahadur, D. Elsworth, Y. Melnichenko, L. He and Y. Wang, Estimation and modeling of coal pore accessibility using small angle neutron scattering, *Fuel*, 2015, **161**, 323-332.
43. S. Liu and R. Zhang, Anisotropic pore structure of shale and gas injection-induced nanopore alteration: A small-angle neutron scattering study, *International Journal of Coal Geology*, 2020, DOI: https://doi.org/10.1016/j.coal.2020.103384, 103384.
44. J. Ilavsky and P. R. Jemian, Irena: tool suite for modeling and analysis of small-angle scattering, *Journal of Applied Crystallography*, 2009, **42**, 347-353.
45. O. Glatter and O. Kratky, *Small angle X-ray scattering*, Academic Press, 1982.
46. Y. Wang, Y. Qin, R. Zhang, L. He, L. M. Anovitz, M. Bleuel, D. F. R. Mildner, S. Liu and Y. Zhu, Evaluation of Nanoscale Accessible Pore Structures for Improved Prediction of Gas Production Potential in Chinese Marine Shales, *Energy & Fuels*, 2018, **32**, 12447-12461.
47. G. Beaucage, Approximations leading to a unified exponential power-law approach to small-angle scattering, *Journal of Applied Crystallography*, 1995, **28**, 717-728.
48. , http://www.sasview.org/.
49. Y. Belmabkhout, M. Frère and G. D. Weireld, High-pressure adsorption measurements. A comparative study of the volumetric and gravimetric methods, *Measurement Science and Technology*, 2004, **15**, 848-858.

50. K. Murata, M. El-Merraoui and K. Kaneko, A new determination method of absolute adsorption isotherm of supercritical gases under high pressure with a special relevance to density-functional theory study, *J Chem Phys*, 2001, **114**, 4196-4205.
51. R. Pini, Interpretation of net and excess adsorption isotherms in microporous adsorbents, *Microporous and Mesoporous Materials*, 2014, **187**, 40-52.

Author contributions

SL and RZ designed the research; RZ and SL performed the research; RZ, LF, TB, and GS conducted the measurements; RZ analyzed and interpreted the data; RZ drafted the manuscript; All authors gave feedback and contributed to the writing of the manuscript.

Acknowledgments

The authors would like to thank Nichole Wonderling for providing the measurement and data analysis of X-ray diffraction at Penn State Materials Characterization Lab. The authors want to thank Yun Liu for the help of vSANS measurement and data reduction at the NIST Center for Neutron Research (NCNR). Access to CHRNS vSANS was provided by the Center for High Resolution Neutron Scattering, a partnership between the National Institute of Standards and Technology and the National Science Foundation under Agreement No. DMR-2010792. This work benefited from the use of the SasView application, originally developed under NSF award DMR-0520547. SasView contains code developed with funding from the European Union's Horizon 2020 research and innovation programme under the SINE2020 project, grant agreement No 654000.

Competing interests

The authors declare no competing financial interests.

Figures

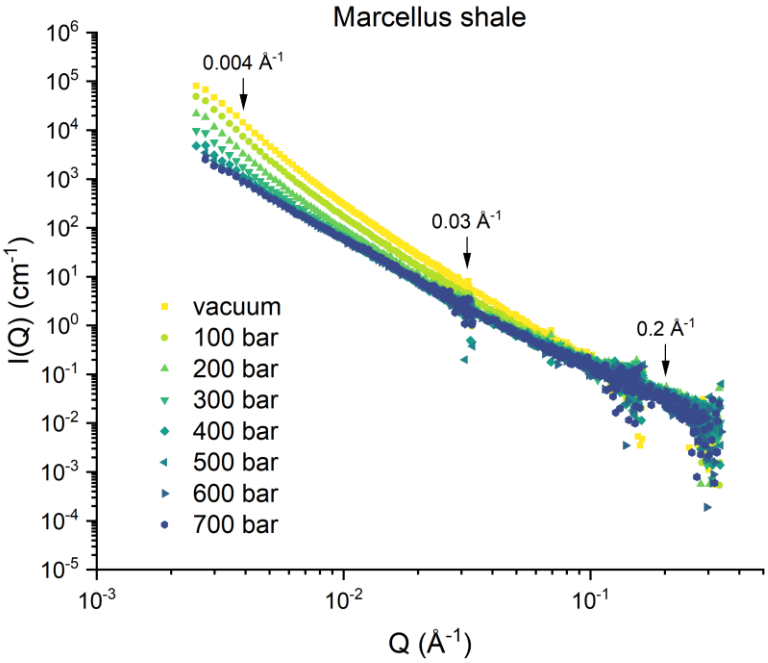

Figure 1 Scattering intensity as a function of methane pressure for the Marcellus shale sample

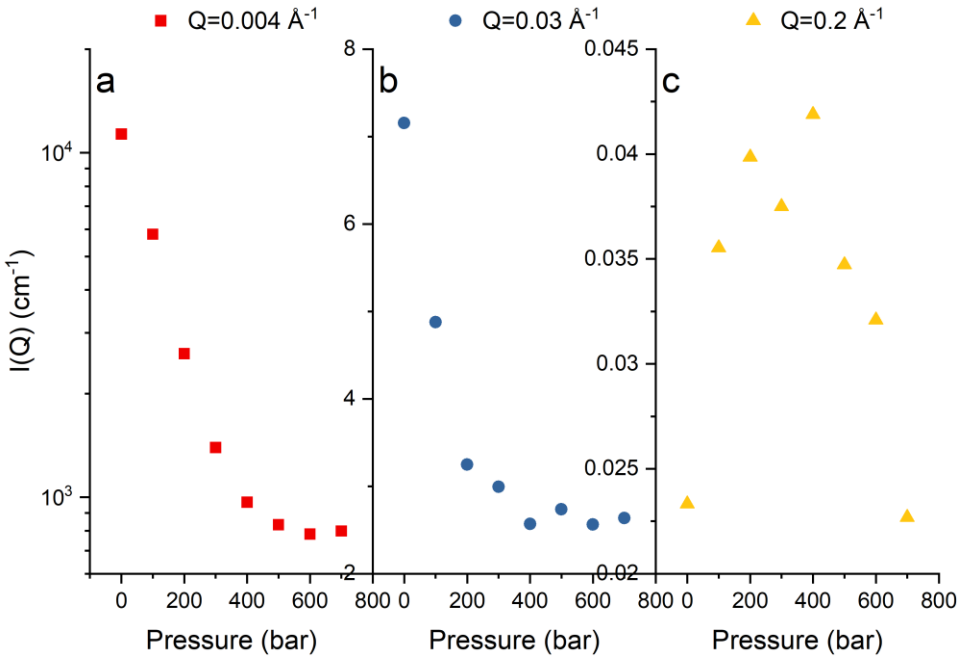

Figure 2 Scattering intensity as a function of methane pressure at **(a)** Q of 0.004 Å^{-1}, **(b)** Q of 0.03 Å^{-1}, and **(c)** Q of 0.2 Å^{-1} for the Marcellus shale sample

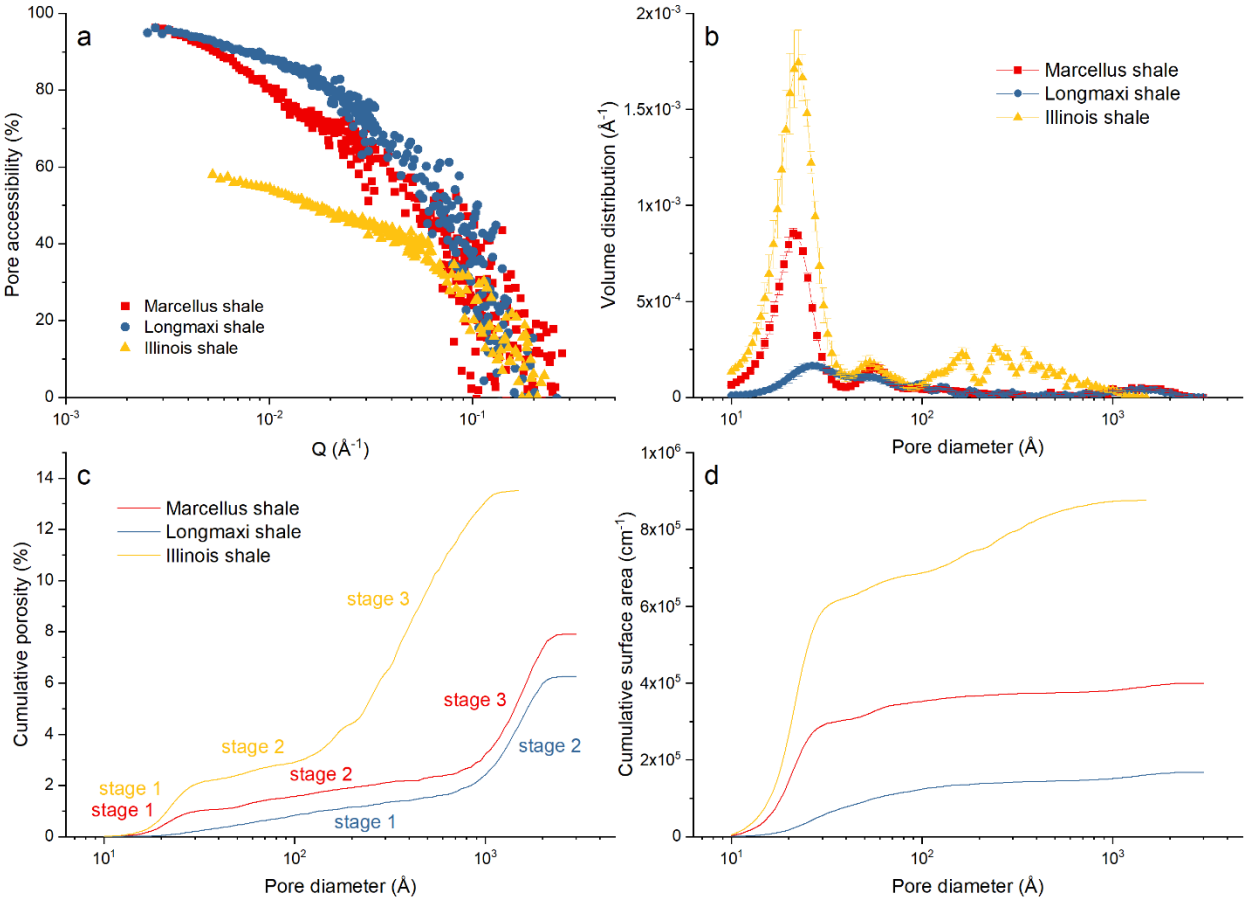

602

603 **Figure 3 (a)** Pore accessibility, **(b)** pore volume distribution, and cumulative **(c)** porosity and **(d)**

604 surface area of the three shale samples

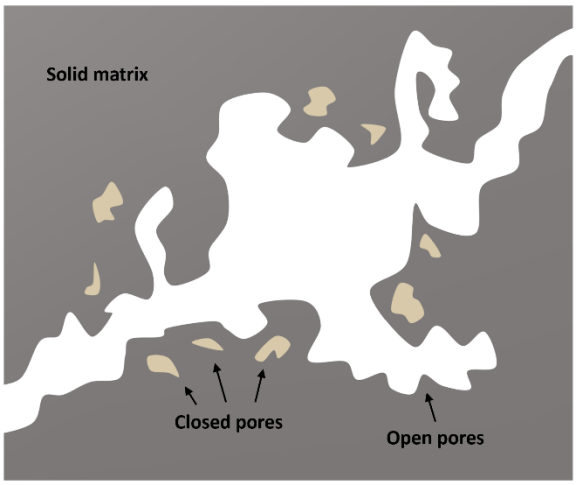

605

606 **Figure 4** A schematic of three-phase system in shale matrix

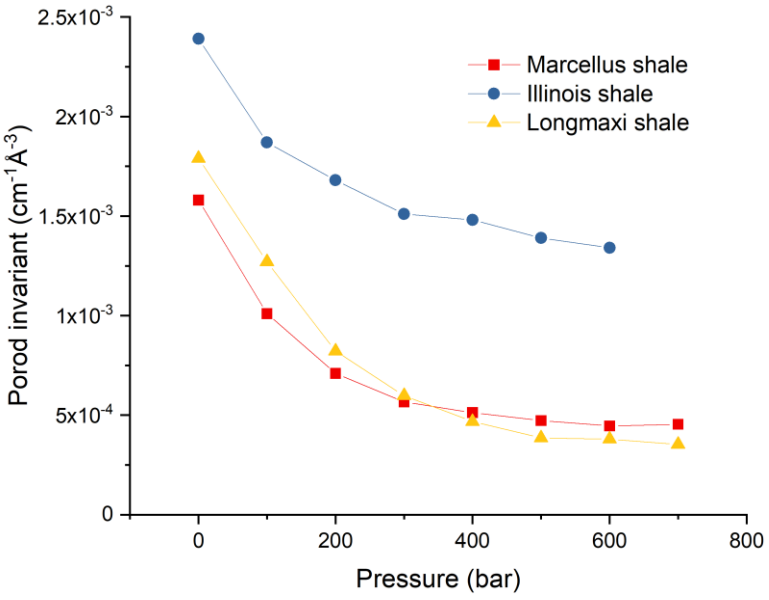

607

608 **Figure 5** Porod invariant as a function of pressure for the three shale samples

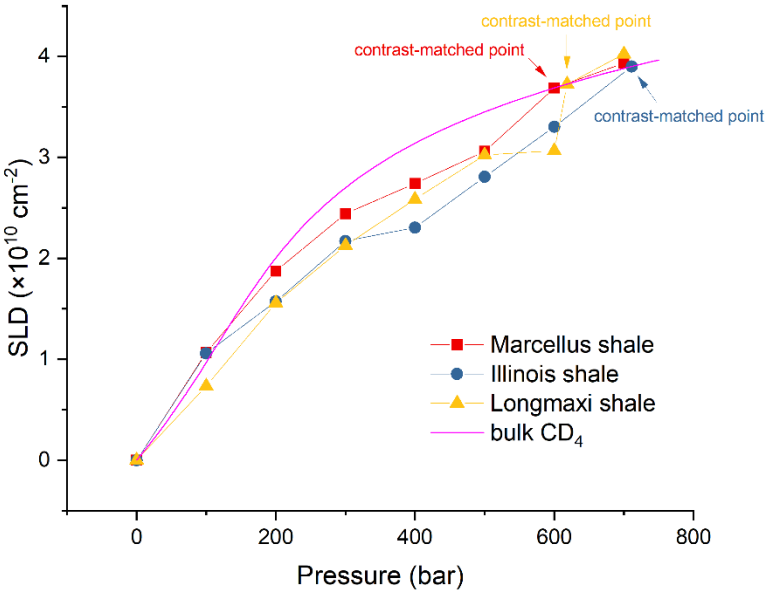

609

610 **Figure 6** Average SLD in open pores as a function of pressure for the three shale samples

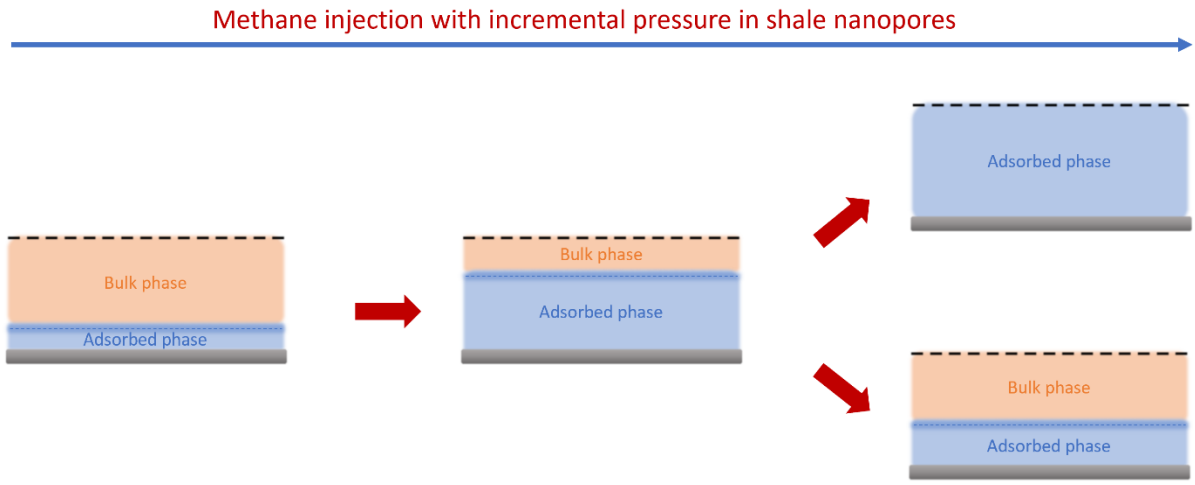

611

612 **Figure 7** Schematics of the hypothetical mechanism of methane sorption and compression as
613 elevating pressure in idealized shale nanopores (The black dashed line is the centerline in pores;
614 the gray area is the shale matrix)

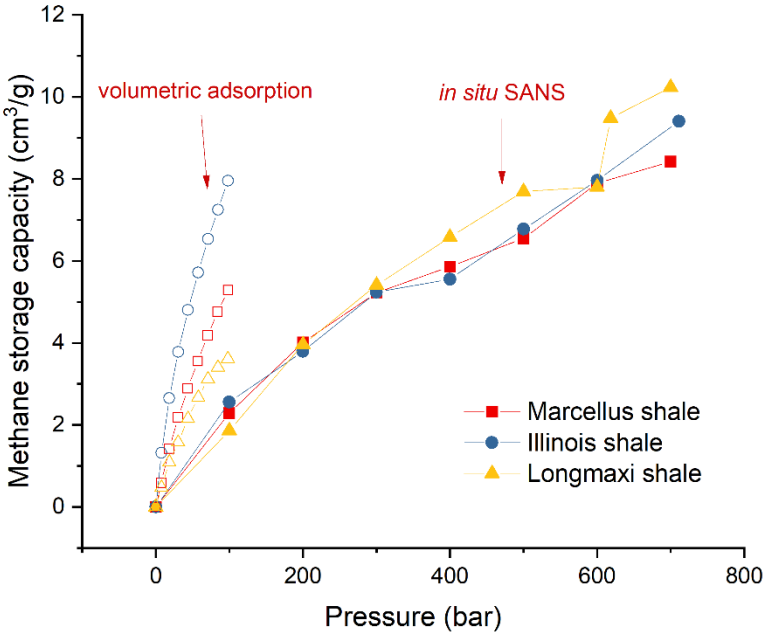

615

616 **Figure 8** Methane storage capacity in open pores as a function of pressure for the three shale
617 samples